reactions

Article

Texturally Modified Zirconia–Tungstophosphoric Acid Catalysts for Efficient Lignocellulosic Pyrolysis

Jose L. Buitrago [1], Leticia Jésica Méndez [1], Mónica Laura Casella [1,2], Juan Antonio Cecilia [3], Enrique Rodríguez-Castellón [3], Ileana D. Lick [1] and Luis R. Pizzio [1,*]

[1] Centro de Investigación y Desarrollo en Ciencias Aplicadas "Dr. J.J. Ronco" (CINDECA) (CONICET CCT-La Plata, UNLP, CICPBA), Departamento de Química, Facultad de Ciencias Exactas, Universidad Nacional de La Plata, CONICET, 47 No. 257, La Plata 1900, Buenos Aires, Argentina; josebuitrago@quimica.unlp.edu.ar (J.L.B.); mendezl@quimica.unlp.edu.ar (L.J.M.); casella@quimica.unlp.edu.ar (M.L.C.); ilick@quimica.unlp.edu.ar (I.D.L.)

[2] Departamento de Ciencias Básicas y Experimentales, UNNOBA, Gaucho Argentino y Ruta Nacional N° 7, Junín 6000, Buenos Aires, Argentina

[3] Departamento de Química Inorgánica Cristalografía y Mineralogía, Facultad de Ciencias, Instituto Interuniversitario de Investigación en Biorrefinerías I3B, Universidad de Málaga, 29071 Málaga, Spain; jacecilia@uma.es (J.A.C.); castellon@uma.es (E.R.-C.)

* Correspondence: lrpizzio@quimica.unlp.edu.ar

Abstract

This work presents the synthesis, characterization, and application of zirconium oxide (ZrO_2)-based catalysts, modified with macro (silica nanospheres, NSP-SiO_2) and mesopore templates (Pluronic 123), impregnated with tungstophosphoric acid (TPA), in the catalytic pyrolysis of tomato agro-industrial residues. The NSP-SiO_2 (SXX) and P123 (PYY) amount mainly influences the ZrO_2SXXPYY-specific surface area (S_{BET}) and average pore diameter (D_p). ^{31}P MAS NMR and FT-IR characterization results show that TPA ($H_3PW_{12}O_{40}$) was partially transformed into $[P_2W_{21}O_{71}]^{6-}$ and $[PW_{11}O_{39}]^{7-}$ during the synthesis steps. The acidic properties of ZrO_2SXXPYY samples containing 25 and 50 wt% of TPA (ZrO_2SXXPYYT25 and ZrO_2SXXPYYT50, respectively) are dependent on both the TPA content and the support nature. Bio-oil composition and product selectivity were strongly influenced by the textural and acid-based properties of the catalysts. Notably, non-catalytic pyrolysis favored pathways leading to C2 compounds, with a high content of acetic acid and hydroxyacetone. In contrast, the use of catalysts promoted the formation of higher molecular weight oxygenated compounds (C5–C6), specifically furans, aldehydes, and ketones.

Keywords: tungstophosphoric acid; heteropolyacids; zirconium oxide; catalytic pyrolysis; furans; acid catalysts

Academic Editors: Diogo M.F. Santos, Catarina Nobre, Paulo Brito and Margarida Gonçalves

Received: 14 January 2026
Revised: 7 March 2026
Accepted: 8 March 2026
Published: 14 March 2026

1. Introduction

Lignocellulosic biomass primarily comprises hemicellulose, cellulose, lignin, and volatile compounds. A significant portion of this biomass is often discarded as waste through agro-industrial activities, with many instances leading to open burning. This practice not only poses health risks but also contributes to global warming [1,2].

The chemical composition of lignocellulosic biomass, including C5 and C6 sugars (from hemicellulose), glucose (from cellulose), and phenolic units (from lignin) makes it a valuable resource for the sustainable production of useful molecules in biorefineries. This

promotes waste transformation via chemical or catalytic processes, allowing for conversion into high-value products [3].

Various transformation routes include chemical or biochemical processes, such as digestion and fermentation. Among thermochemical processes, carbonization, combustion, liquefaction, and pyrolysis, which operate at high temperatures under controlled conditions, are often used.

Globally, tomatoes are one of the most cultivated crops, with an annual production exceeding 180 million tons [4]. This generates a massive volume of lignocellulosic residues (stems and leaves) that are typically underutilized or burned in open fields. Therefore, using tomato waste as a model substrate is highly relevant for developing sustainable biorefinery protocols that are applicable to diverse agro-industrial regions worldwide [5]. In Argentina, approximately 19,532 hectares are dedicated to tomato cultivation, yielding around 15 tons of waste per hectare [6,7].

This considerable volume of agricultural waste presents an opportunity for conversion into valuable products through thermochemical technologies. Biomass pyrolysis stands out for its capability to convert lignocellulosic waste into liquid, solid, and gaseous fractions. Among these, bio-oils are particularly valuable due to their potential as a precursor for biofuels and renewable chemical compounds.

Pyrolysis is a thermochemical process performed in a controlled, typically inert atmosphere [8,9]. It can be categorized into three main types:

1. Fast pyrolysis: Biomass decomposes quickly at high temperatures, releasing volatile compounds and forming a solid carbon-rich residue. Bio-oils are formed from the condensation of condensable gases.
2. Slow pyrolysis: This operates at lower temperatures and longer residence times, focusing more on solid product yield.
3. Flash pyrolysis: This is characterized by very rapid heating and short residence times.

Even with its advantages, bio-oil fractionation poses significant barriers to its industrial application due to the high oxygen content and complex molecular diversity of the resulting bio-oils. Despite the testing of numerous catalysts, there remains a lack of research concerning the rational design of multimodal zirconia supports that are capable of concurrently enhancing mass transport through macropores and enhancing selectivity toward platform molecules (C5–C6) via regulated acidic sites [10,11].

Catalytic pyrolysis can be employed to enhance the quality and yield of bio-oils and reduce the number of molecules in them. There are two types of catalytic pyrolysis: in situ or ex situ catalytic pyrolysis. In the first one, the catalyst is present in the same bed as the biomass, enabling direct interaction between the concentrated vapors, while in the second one, the catalyst is in a separate bed, allowing for the primary vapors from pyrolysis to interact with the catalyst, simplifying its separation from solid residues [12].

A variety of materials are used as catalysts in biomass pyrolysis. Supports that allow the addition of acidic compounds are commonly sought to enhance catalytic efficiency and selectivity. Common supports include zeolites, metal oxides, and activated carbons. The addition of acid sites can help to manage selectivity and promote several reactions such as depolymerization, cracking, dehydration and decarboxylation [13–15].

Zirconium oxide (ZrO_2) is particularly interesting, due to its high thermal stability and surface properties that are determined by different crystal structures. It also has controllable acid-base and textural properties. The addition of compounds that confer acidity, such as Keggin-type heteropolyacids, to this type of support can increase catalytic activity in processes such as dehydration [16].

With regard to the use of ZrO_2 in the catalytic pyrolysis of biomass, Jin et al. used a combination of stage catalysts with Al-MCM-41, HZSM-5, and ZrO_2 to improve the quality

and yield of the bio-oils obtained from the pyrolysis of sawdust. These authors highlight the critical influence of ZrO_2 in the ex situ catalytic pyrolysis efficiency. Incorporating ZrO_2 led to an increase in the yield of heavy organics and also markedly enhanced the selectivity for monoaromatic hydrocarbons [17]. Moreover, Hernando et al. studied nanocrystalline ZSM-5 catalysts, modified by the incorporation of ZrO_2 and agglomerated with attapulgite (ZrO_2/n-ZSM-5-ATP) for biomass pyrolysis. These authors demonstrated that materials containing ZrO_2 improved the quality of bio-oils from various lignocellulosic biomasses by promoting deoxygenation reactions [18].

Although few studies have reported results on the catalytic pyrolysis of tomato plant residues [19–21], it is generally known that this substrate, in addition to being abundant, has the potential to generate pyrolytic bio-oils that are rich in high-value compounds. In a previous study conducted in our laboratory, the effect of modifying pore size and incorporating acid sites on the yield and composition of bio-oils derived from tomato plant residues was demonstrated [22]. Overall, it was found that modifying the support mesoporosity substantially altered the composition of the bio-oils.

This study aims to design ZrO_2-based catalysts by tailoring their physical and chemical properties and to evaluate their performance in the pyrolysis of tomato plant waste. The ZrO_2 catalysts were synthesized using the sol–gel method and modified with two pore-forming agents: NSP–SiO_2, employed as a macropore former, and Pluronic P123, used as a mesopore former. These modifications yielded materials with distinct textural and structural characteristics.

To introduce acidic properties, the catalysts were impregnated with tungstophosphoric acid (TPA), a Keggin-type heteropolyacid. The purpose of this work is to determine whether the formation of valuable compounds in the resulting bio-oils is primarily governed by diffusion and confinement effects, catalytic transformations at acidic sites, or surface-mediated rearrangements. The findings will contribute to a deeper understanding of the structure–function relationships involved in the catalytic valorization of biomass waste.

2. Materials and Methods

2.1. Catalysts Preparation

Materials based on zirconia with different pore former proportions were synthesized to achieve a multimodal oxide structure. Pluronic P123 (Poly(ethylene glycol)-block-poly(propylene glycol)-block-poly(ethylene glycol), $PEO_{20}PPO_{70}PEO_{20}$) and silica nanospheres (NSP-SiO_2) synthesized by the Stöber method [23] were used as meso- and macropore-forming agents.

A solution was prepared by dissolving 13.3 g of zirconium propoxide (Sigma-Aldrich, St. Louis, MO, USA) in 168 g of ethanol (Merck, Darmstadt, Germany) under a N_2 atmosphere at room temperature.

After 30 min, an appropriate amount of Pluronic P123 (Sigma-Aldrich, St. Louis, MO, USA) and NSP-SiO_2 was added to the hydrolyzed solution under vigorous stirring, as templates. The P123 and NSP-SiO_2 amounts were chosen to obtain different weight percentages of meso- and macropore templates. After 3 h, the stirring stopped and the suspension was aged 24 h at 90 °C. The solid was ground into powder and washed with a sodium hydroxide solution to remove SiO_2 templates under constant stirring for 24 h. The material was then washed with deionized water to remove the sodium from the solid until a neutral pH was reached. The P123 template was removed by ultrasonic treatment for one hour at room temperature. The samples were named ZrO_2SXXPYY, where XX and YY represent the weight percentage of SiO_2 and P123 used during the synthesis, respectively.

The ZrO_2SXXPYY materials were used as TPA support. The impregnation was performed by contacting, at room temperature, 0.75 g (or 0.50 g) of the support with 0.25 g

(or 0.50 g) of tungstophosphoric acid ($H_3PW_{12}O_{40}$) (Sigma-Aldrich, St. Louis, MO, USA) dissolved in 3 mL of water–ethanol 50 vol% solution to obtain a TPA concentration of 25 wt% or 50 wt% in the final material (named ZrO_2SXXPYYT25 and ZrO_2SXXPYYT50, respectively). Finally, the solids were calcined at 450 °C for 2 h under the air atmosphere to ensure the complete removal of any residual P123 template and to stabilize the supported HPA phase. The procedure used to determine the TPA content in the calcined materials is described in the Supplementary Material.

2.2. Catalyst Characterization

The nitrogen adsorption/desorption measurements were carried out at liquid nitrogen temperature (−196 °C), using Micromeritics ASAP 2020 equipment (Norcross, GA, USA). From the obtained data, the specific surface area (S_{BET}) was determined using the Brunauer–Emmett–Teller model, the micropore area (S_{MIC}) by the t-plot method, and the mean pore diameter (D_p) and the pore size distribution by the BJH method. The species present in the supports and catalysts were evaluated by FT-IR, using a Bruker IFS 66 (Billerica, MA, USA) with pellets of the sample in KBr, in the 400–4000 cm^{-1} range at room temperature. The X-ray diffraction (XRD) patterns were recorded with Panalytical X'Pert PRO (Worcestershire, UK) equipment with a built-in recorder, using Cu Kα radiation, a nickel filter, 20 mA and 40 kV in the high voltage source, and a scanning angle between 5 and 60° 2θ at a scanning rate of 1° per min. The acid strength and the number of acid sites were estimated from the *n*-butylamine potentiometric titration results obtained using a Metrohm 794 Basic Titrino apparatus (Herisau, Switzerland) with a double junction electrode.

The mean size and size distribution of the NSP-SiO_2 were estimated using SEM micrographs obtained using an ESEM FEI Quanta 250 microscope using ADDAII acquisition device (FEI Company, Hillsboro, OR, USA), with a Soft Imaging System 5.1, at a magnification of 10,000×, measuring a few hundred spheres. For sample preparation, a small amount of the synthetized material was placed on a carbon ribbon and coated with gold by sputtering.

The solids were analyzed by ^{31}P magic angle spinning-nuclear magnetic resonance (MAS-NMR) spectroscopy. For this purpose, Bruker MSL-300 equipment (Billerica, MA, USA) was employed, using 5 ms pulses, with a 60 s delay, and working at a frequency of 121.496 MHz for ^{31}P at room temperature; the resolution was 3.052 Hz per point. A 5 mm diameter and 10 mm high sample holder was used; the spin rate was 2.1 kHz. Several hundred pulse responses were collected. Phosphoric acid with a concentration of 85% was employed as an external reference.

The chemical state and chemical composition of the surface of the studied materials were studied by X-ray photoelectron spectroscopy (XPS) on a PHI Versa-Probe II Scanning XPS Microprobe (Physical Electronics) spectrometer (Eden Prairie, MN, USA). X-ray sources (Al Kα; hν = 1486.6 eV) operating at 100 W and 20 kV under a vacuum of 10^{-7} Pa were used. The PHI SmartSoft software 4.3.1 and the MultiPak 9.3 package were used for fitting the XPS spectra. The binding energy of the C 1*s* core level at 284.8 eV arising from the adventitious carbon was used to calibrate the spectra.

The lignocellulosic biomass was obtained from tomato producers in La Plata, Buenos Aires, Argentina. Aerial remains of tomato plants (*Solanum lycopersicum* L.) of the local variety known as 'tomate platense' were used. The samples were collected through a sampling and quartering process from a total sample of 10 kg. Only leaves and stems were used, which were crushed to obtain particles with a diameter between 0.415 and 1 mm by sieving them with steel meshes. The composition of hemicellulose, cellulose and lignin in raw tomato plant leaves and stems was determined using the Van Soest method [24,25] with an ANKON 200 FIBER ANALYZER (Macedon, NY, USA). The moisture content was

determined by gravimetry, drying the samples at 105 °C for 24 h. The mineral components were evaluated by quantifying the ash content through the incineration of aliquots of material in a muffle furnace at 900 °C.

Pyrolysis tests were performed using the previously described biomass under a nitrogen flow of 200 mL min^{-1} at 450 °C in a flow down fixed-bed stainless steel tubular reactor, as shown in the Supplementary Material. The biomass and catalysts were placed between quartz wool plugs to retain solid products and allow for the vapors to pass through in an ex situ catalytic configuration. The operating conditions were selected based on the preliminary TGA results of the biomass.

The experimental setup consisted of a vertical electric furnace equipped with a temperature controller, into which the down-flow fixed bed stainless steel tubular reactor was inserted. For catalytic pyrolysis assays, 1 g of biomass and 0.5 g of the catalyst were loaded into the reactor and separated by a quartz wool layer (see Supplementary Material Figure S1 Schematic diagram of the experimental setup for the ex situ catalytic pyrolysis of tomato plant residues). The reactor was then rapidly introduced into the isothermal zone of the furnace (~2 s), which was preheated to 450 °C. With this procedure, the reactor is a stainless-steel tubular reactor (ID = 1 cm, L = 10 cm in the isothermal zone). The heating rate (225 °C s^{-1}) was verified using a thermocouple centered in the biomass bed. The 0.5 s residence time was calculated based on the effective volume of the catalytic bed.

The vapors generated during pyrolysis were condensed in an ice–salt–water bath to collect the resulting bio-oil. After completion of the reaction, the reactor was withdrawn from the furnace and cooled under an inert atmosphere to prevent the combustion of the remaining solids. Four main product fractions were obtained: (i) bio-oil (condensed fraction), (ii) solid residue/wax (solids retained in the condenser), (iii) biochar (solid residue remaining in the reactor), and (iv) non-condensable gases.

The yields of bio-oils, wax, biochar, and non-condensable gas were determined gravimetrically and calculated as a weight percentage, relative to the initial biomass feed. The following equations (Equations (1)–(4)) were employed:

$$\text{Yield [wt\%](bio-oils)} = \{(\text{weight of the bio-oils collected})/(\text{weight of biomass feed}) \times 100\} \quad (1)$$

$$\text{Yield [wt\%](wax)} = \{(\text{weight of the wax collected})/(\text{weight of biomass feed}) \times 100\} \quad (2)$$

$$\text{Yield [wt\%](biochar)} = \{(\text{weight of the biochar collected})/(\text{weight of biomass feed}) \times 100\} \quad (3)$$

$$\text{Yield [wt\%](non-condensable gas)} = \{100 - (\text{Yield [wt\%](bio-oils)} + \text{Yield [wt\%](biochar)} + \text{Yield [wt\%](wax)}\} \quad (4)$$

The bio-oil was analyzed by GC–MS, using a Shimadzu GCMS-QP2010SE system (Chiyoda-ku, Tokyo, Japan) coupled to a mass spectrometry detector and equipped with a Supelco SPB™-5 capillary column (Millipore Sigma, Burlington, MA, USA) (30 m × 0.25 mm × 0.25 µm). Semi-quantitative analysis was carried out on the assumption that the peak areas are proportional to the concentration of the corresponding compound in the sample. The data were reported, considering a relative error of 2%. A cut-off of 1% was used for the analyses (Areas > 1%).

The GC-MS data were processed using GC-MS Solution software version 4.42. Chromatographic peaks were integrated, and compounds were identified by comparing their mass spectra with the software library. A matching criterion of >95% was applied for identification. Due to similar fragmentation patterns, structural isomers were not differentiated and were aggregated under their corresponding chemical identities. The quantitative results are expressed as relative area [%], calculated by the ratio of the individual peak area to the total integrated area. It is important to note that this semi-quantitative approach assumes similar response factors for all compounds. The compounds were aggregated into

chemical families (e.g., acids, furans, phenols) by summing the relative areas of their constituents. Peaks with a relative area below 2%, as well as unidentified compounds, proteins, lignin derivatives, and plant-derived fatty acids, were grouped in the 'Others' category.

3. Results

3.1. Biomass Characterization

The residual biomass used as a substrate in this study consists mainly of stems and leaves from tomato plant waste collected from a plantation located in La Plata, Buenos Aires, Argentina. The results of the compositional analysis showed that the material has a typical composition for this kind of waste (27.5% cellulose, 16.5% hemicellulose and 8.2% lignin). The remaining percentage corresponds to extractive compounds, which include a wide variety of substances such as proteins, flavonoids, fatty acids, terpenes, and other secondary metabolites. These components can influence the composition of the obtained bio-oils because they are highly susceptible to thermal degradation and can give rise to volatile products with added value during pyrolysis. On the other hand, cellulose and hemicellulose, when subjected to thermal degradation, contribute significantly to the generation of oxygenated compounds in the liquid phase, while lignin, which is more recalcitrant, is a potential source of aromatic compounds [26,27].

The moisture and ash contents determined were 10.2% and 10.4%, respectively. Moisture represents the water physically retained in the biomass, while ash reflects the inorganic content, which is mainly associated with minerals that are naturally present in the plant material.

As we previously reported [22], thermogravimetric analysis of tomato stem and leaf residues revealed losses associated with water release (from room temperature to 100–115 °C); volatile constituent elimination (from 115 to 190 °C); hemicellulose, which can degrade at around 150 °C according to the literature; and cellulose, which degrades between 200 and 450 °C, with maximum degradation occurring between 290 and 380 °C [28].

3.2. Materials Characterization

According to the SEM micrograph (Figure 1a), the NSP-SiO_2 nanospheres present a smooth surface and are well dispersed without the formation of silica aggregates. The average diameter of the nanospheres was found to be 293.8 ± 17.5 nm (Figure 1b). These spheres were used as templates in the ZrO_2SXXPYY synthesis, using weight percentages of 25 and 50%.

SEM analysis of the ZrO_2 sample (Figure 1c) reveals a compact structure formed by particles with irregular morphology and a wide size distribution (ranging from 134 to 790 nm). The ZrO_2P25 sample micrograph (Figure 1d), obtained by adding P123 (25 wt%) during the synthesis, displays a looser structure formed by spherical particles with a homogeneous particle size distribution (mean size 345 ± 78 nm).

The images of the ZrO_2SXXPYY materials after the treatments were performed to remove the NSP-SiO_2 and P123 templates (Figure 1e) show the voids on the zirconia surface generated by the silica nanospheres removal. They are more visible in the samples prepared using the higher template proportions. The voids' average diameters (372 ± 64 nm) were slightly higher than that of NSP-SiO_2.

The classical method to assess macropore size is mercury porosimetry. However, this technique presents several drawbacks: among them are their destructive nature (samples cannot be reused after analysis), toxicity, and environmental hazards [29].

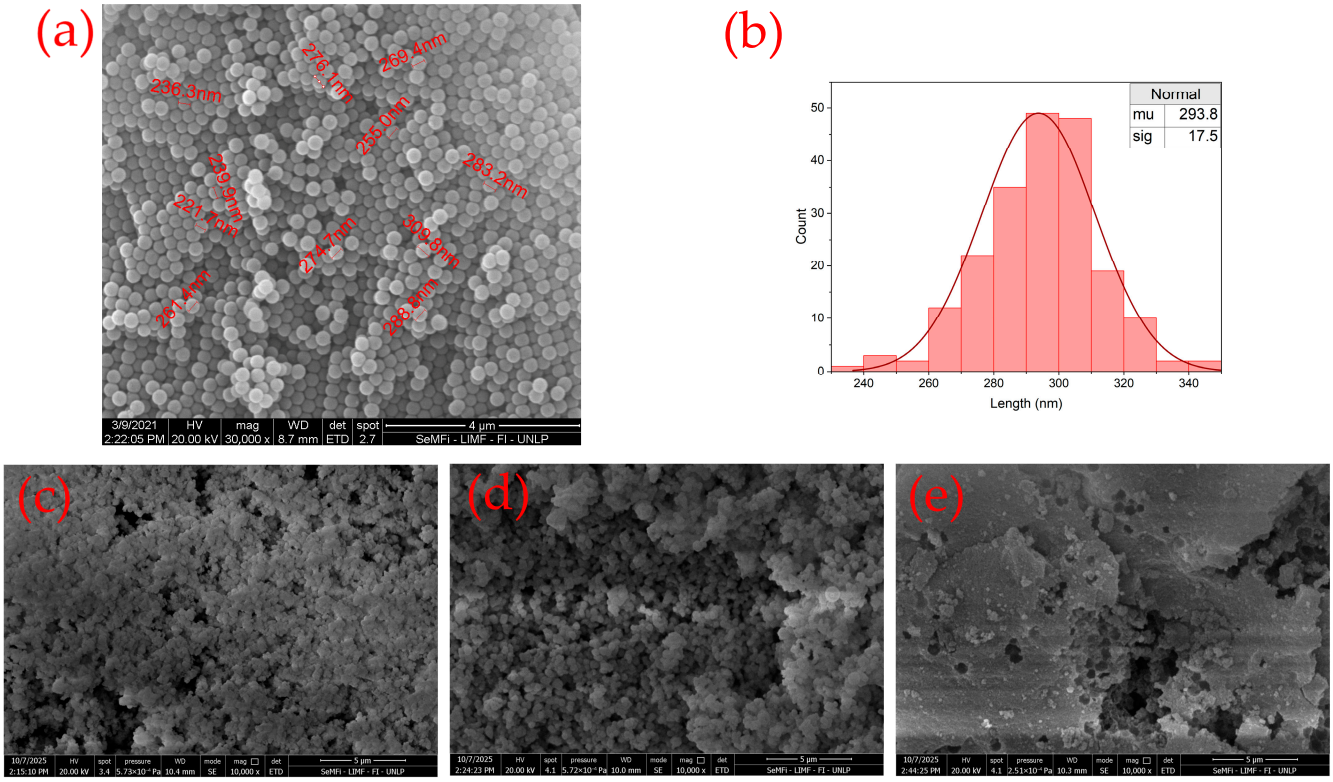

Figure 1. SEM micrographs of NSP-SiO_2 (**a**), NSP-SiO_2 particle size distribution histograms based on SEM images (**b**), and SEM micrographs of ZrO_2 (**c**), ZrO_2P25 (**d**), and ZrO_2S25P50 (**e**) samples.

The specific surface area (S_{BET}) determined from the N_2 adsorption–desorption isotherms using the Brunauer–Emmett–Teller (BET) method, the average pore diameter (D_p), and the pore volume (V_p) of ZrO_2SXXPYY samples are summarized in Table 1.

Table 1. Textural properties ZrO_2SXXPYY synthesized materials.

Sample	NSP-SiO_2 (wt%)	P123 (wt%)	S_{BET} (m^2 g^{-1})	S_{MIC} (m^2 g^{-1})	S_{MESO} (m^2 g^{-1})	V_p * (cm^3 g^{-1})	D_p (nm)
ZrO_2	0	0	213	162	51	0.14	3.0
ZrO_2S25	25	0	69	3	66	0.19	3.7
ZrO_2P25	0	25	192	15	177	0.19	3.7
ZrO_2S25P25	25	25	181	8	173	0.18	3.6
ZrO_2S50P25	50	25	141	4	137	0.25	6.9
ZrO_2S25P50	25	50	157	0	157	0.45	10.8

* Estimated from the value corresponding to P/P_0 = 0.98.

The reference sample ZrO_2, synthesized without the addition of pore templates, showed N_2 adsorption–desorption isotherms (Figure S2 N_2 adsorption–desorption isotherm, Supplementary Material) that were typical of micro–mesoporous materials (S_{MICRO} = 162 and S_{MESO} = 51 m^2 g^{-1}**)** and can be classified as type IV with an H_2 hysteresis loop, according to IUPAC classification [30]. The pore size distribution reveals the presence of micropores and small mesopores (in the range of 4–6 nm).

The incorporation of NSP-SiO_2 as a macroporous template during the ZrO_2S25 synthesis resulted in a notorious S_{BET} value reduction (69 m^2 g^{-1}, almost entirely due to mesopores) and a pore volume increase (0.19 cm^3/g). The S_{BET} and V_p ascribed to macropores cannot be revealed by this technique, and they were estimated (~2 m^2 g^{-1} and 0.09 $cm^3 g^{-1}$, respectively), taking into account an average nanosphere diameter that was equal to 294 nm. The PSD shows small mesopores (centers at approximately 2.0 nm) and large mesopores (in the range of 10–40 nm).

In comparison with ZrO_2 (the reference sample), as a result of mesopore template incorporation (ZrO_2P25 sample), S_{BET} slightly decreases and both V_p and D_p increase. However, more than 90% of the specific surface area for this sample is due to its mesoporous structure (S_{MICRO} = 15 and S_{MESO} = 177 m^2 g^{-1}**).** The pore size distribution shows the presence of mesopores with a size of less than 10 nm, mainly in the range of 2–6 nm (centers at approximately 3.0 nm).

The ZrO_2S25P25 sample, which was synthetized using both templates, showed high S_{BET} (181 m^2 g^{-1}), with a negligible micropore contribution (V_p = 0.18 cm^3 g^{-1} and D_p = 3.6 nm). The PSD shows an increment of the mesopores in the range of 6–10 nm increase, assigned to the NSP-SiO_2 addition. The increments could be due to the presence of voids generated by the unordered stacking of silica nanospheres, which can be partially filled by P123. As a result of the NSP-SiO_2 amount increment (keeping the P123 content constant), the ZrO_2S50P25 sample S_{BET} decreases (S_{BET} = 141 m^2 g^{-1}, without micropore contribution), and again, both V_p and D_p increase (0.25 cm^3 g^{-1} and 6.9 nm, respectively). However, for the ZrO_2S25P50 sample (S_{BET} = 157 m^2 g^{-1}), higher V_p and D_p increments were achieved (0.45 cm^3 g^{-1} and 10.8 nm, respectively), increasing the P123 content but keeping constant the NSP-SiO_2 amount. The pore size distribution of this sample shows a wide range (4–40 nm) of mesopore distribution with a maximum of ~10 nm.

The effect of the kind and amount of template used on the pose size distribution can be seen in Figure S3 Pore size distribution.

The TPA and most of its salts [except Cs, Rb and K ones] present negligible specific surface area values [<10 m^2 g^{-1}]. This fact is considered a drawback when they are used as heterogeneous catalysts and can be overcome by immobilizing TPA on a solid support with a high specific surface. The materials obtained by TPA impregnation show lower S_{BET} values than the parent solids used as support. For the ZrO_2SXXPYYT25 samples, the specific surface area value drops can be mainly explained by considering that the S_{BET} of bulk TPA is very low (<2 m^2 g^{-1}), and its proportions in ZrO_2SXXPYYT25 and the sample ZrO_2SXXPYYT50 materials are 25% and 50%, respectively. In addition, it could also be attributed to the micro-mesopores blocking of the ZrO_2SXXPYY supports by the TPA anion (main diameter 1.2 nm). For example, due to the impregnation of ZrO_2 with 25 wt.%, the S_{BET} was reduced by approximately 60%, in this case as result of the S_{MIC} drop (from 162 to 25 m^2 g^{-1}). The S_{BET} reduction varies by a range of 54–87% (see Table S1), being the highest for the solid sample with 50 wt.% of TPA (ZrO_2S25P25T50)

As was previously reported for ZrO_2 and ZrO_2P25 materials [22], the XRD patterns of ZrO_2S25, ZrO_2S25P25, ZrO_2S50P25, and ZrO_2S25P50 samples exhibited a broad peak at 2θ~32°, which was indicative of low zirconia crystallinity.

The FT-IR spectrum of the ZrO_2 sample (Figure S4 FT-IR spectrum of synthesized materials) showed the bands assigned to the stretching vibrations of hydroxo and aquo-OH (3455 cm^{-1}), and to the bending vibration of the H_2O and Zr-O-H species, placed at 1637 and 1385 cm^{-1} [31,32].

Additionally, the broad band associated with the Zr-O stretching vibration was observed in the energy range below 850 cm^{-1} [31]. For the samples synthetized using P123, the FT-IR spectra showed weak signals at 1081, 1055, and 850 cm^{-1}, which are assigned to the template C-O-C/C-O-H stretching and CH_2 rocking vibrations, respectively. This fact indicates that the ultrasound treatment and subsequent calcination at 450 °C did not completely remove P123. Taking into account that the materials were evaluated at the same temperature (450 °C) for 5 min, it can be ruled out that the P123 traces can potentially affect the product distribution [33].

The FT-IR analysis of ZrO_2SXXPYYT25 and ZrO_2SXXPYYT50 materials reveals the presence of the main TPA bands located at 1081, 982, 888, and 793 cm^{-1} (assigned to

the P-Oa, W-Od, W-Ob-W, and W-Oc-W stretching vibrations, respectively) [34], which overlap with those of the support. The intensity of these bands increases with the TPA content increment. The FT-IR spectra also show bands at 1101, 1059, 957, and 818 cm^{-1}, assigned to the lacunar $[PW_{11}O_{39}]^{7-}$ anion. The $[PW_{12}O_{40}]^{3-}$ anion could undergo partial transformation into the lacunar anion during the synthesis and drying steps due to its limited stability. The intensity of those bands seems to be higher for the ZrO_2 P25T25, ZrO_2S25T25, ZrO_2S50P25T25, and ZrO_2S25P50T25 samples.

^{31}P MAS NMR spectrum of bulk hydrated TPA exhibits only one narrow peak at −15.3 ppm (line width ~ 0.04 ppm), assigned to the deprotonated $[PW_{12}O_{40}]^{3-}$ Keggin anion [35] that interacts with $H^+(H_2O)_2$ species.

In the case of the ZrO_2SXXPYYTPA materials (Figure 2), the ^{31}P MAS-NMR spectra showed a peak that was slightly wider at −15.1 ppm (line width ~ 0.5 ppm). The increase can be assigned to W-O-Zr bonds formation, as a result of the thermal treatment, through the following path (Equations (5)–(7)) [36]:

$$[Zr\text{-}OH_2^+][PW_{12}O_{40}]^{3-} \rightarrow [Zr\text{-}O\text{-}W\text{-}PW_{11}O_{39}]^{2-} + H_2O \quad (5)$$

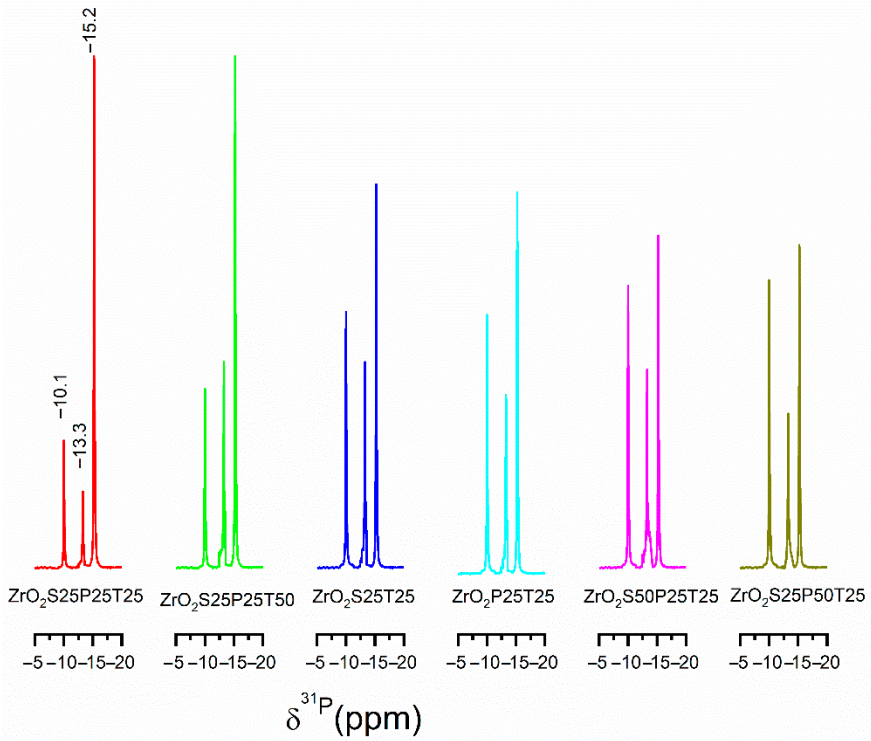

Figure 2. ^{31}P MAS-NMR spectra of ZrO_2S25P25T25, ZrO_2S25P25T50, ZrO_2S25T25, ZrO_2P25T25, ZrO_2S50P25T25, and ZrO_2S25P50T25 samples.

During the impregnation and drying steps, the $[PW_{12}O_{40}]^{3-}$ anions interact electrostatically with the positively charged species ($Zr\text{-}OH_2^+$) that are present on the ZrO_2SXXPYY surface:

$$[PW_{12}O_{40}]^{3-} + 3(H_2O)_2H^+ + nZr\text{-}OH \rightarrow [Zr\text{-}OH_2^+]_n[H_{3-n}PW_{12}O_{40}]^{n-} + 3H_2O \quad (6)$$

For the ZrO_2S25P25T25 and ZrO_2S25P25T50 samples, the spectra also show the presence of two peaks at −13.3 ppm and 10.1 ppm, ascribed to the $[P_2W_{21}O_{71}]^{6-}$ and $[PW_{11}O_{39}]^{7-}$ species, respectively [37]. The intensities of those peaks were lower than the one assigned to $[PW_{12}O_{40}]^{3-}$ anion.

The ZrO_2S25T25, ZrO_2P25T50, ZrO_2S50P25T25, and ZrO_2S25P50T50 ^{31}P MAS-NMR spectra reveal that the intensities of the peaks assigned to the dimeric and lacunar species increase; however, they are still lower than that of the $[PW_{12}O_{40}]^{3-}$ anion.

According to the ^{31}P MAS-NMR results, the main species present in ZrO_2S25P25T25 and ZrO_2S25P25T50 samples is the $[PW_{12}O_{40}]^{3-}$ anion. However, it was partially transformed into $[P_2W_{21}O_{71}]^{6-}$ and $[PW_{11}O_{39}]^{7-}$ anions during the synthesis and drying steps. The $[PW_{12}O_{40}]^{3-}$ transformation degree increases for the other materials. Due to the limited stability of the $[PW_{12}O_{40}]^{3-}$ anion in solution, at pH 1.5–2.0, it could be reversibly transformed into the lacunar species $[PW_{11}O_{39}]^{7-}$. It was proposed [38] that the transformation occurs through the following scheme when the pH increases:

$$[PW_{12}O_{40}]^{3-} \Leftrightarrow [P_2W_{21}O_{71}]^{6-} \Leftrightarrow [PW_{11}O_{39}]^{7-} \quad (7)$$

We have reported that the $[PW_{12}O_{40}]^{3-}$ transformation can occur during the materials synthesis steps (impregnation and thermal treatment). It was also reported that when more basic materials are used as support, the dimeric and lacunar species proportion becomes more important [39]. So, as was revealed by ^{31}P MAS-NMR, the less acidic samples (ZrO_2P25, ZrO_2S25, ZrO_2S50P25, and ZrO_2S25P50) give rise to a higher dimeric and lacunar species proportion.

The fact that the FT-IR bands of the dimeric anion are similar to those of $[PW_{12}O_{40}]^{3-}$ is the reason why we could not identify it.

Bulk TPA is a purely Brønsted acid. When supported on ZrO_2, the interaction between the HPA and the surface hydroxyl groups (Zr-OH) can generate a combination of both site types. The presence of lacunar species ($[PW_{11}O_{39}]^{7-}$) and dimeric anions ($[P_2W_{21}O_{71}]^{6-}$), as evidenced by ^{31}P MAS NMR, suggests a significant contribution of the Lewis acidity. These species often coordinate with Zr^{4+} cations from the support, which act as Lewis acid sites (electron-pair acceptors). This combination of both Brønsted and Lewis acidity is a key feature of ZrO_2SXXPYYT25 and ZrO_2SXXPYYT50 catalysts, playing a crucial role in the dehydration and selective cracking pathways during the pyrolysis process.

For the materials used as TPA support (ZrO_2SXXPYY samples), the XRD patterns exhibited a broad peak at 2θ~32°, which was indicative of low zirconia crystallinity (see Figure 1).

Moreover, the XRD pattern of the impregnated materials (ZrO_2SXXPYYT25 and ZrO_2SXXPYYT50 samples) exhibited a series of broad and weak reflections that could be assigned to the presence of small $H_3PW_{12}O_{40}$ crystals. However, the weak peak intensities suggest that TPA is predominantly either dispersed on the support in an amorphous state or exists as crystalline domains that are below the detection limit of this technique [40].

Potentiometric titration curves were performed to estimate the acidic properties of the synthetized materials (Figure S5 Potentiometric titration curves of synthesized materials). The initial electrode potential (Ei) was used to estimate the acid sites' strength (see the classification scale in Supplementary Material) and the area under the curve provides an estimation of the number of acid sites (N_{AS}). The Ei and N_{AS} values are shown in Table 2.

It can be observed that the ZrO_2 display a higher Ei value (60 mV) than the other ZrO_2SXXPYY materials used as TPA support. The Ei value drop could be due to the presence of pore templates remaining in the materials. Additionally, it could be ascribed to the presence of sodium ions (which was corroborated by X-ray photoelectron spectroscopy) on the support, because of the treatment with NaOH during the preparation to remove the templates (Table S2 Surface Na/Si atomic ratios of the ZrO2S25, ZrO_2S25T25, ZrO_2S25P25, ZrO_2S25P25T25, and ZrO_2S25P25T50 materials determined by XPS in the Supplementary Material).

Table 2. Surface acidity (NAS) and initial potential (Ei) of the synthesized ZrO_2-based samples.

Sample	N_{AS} (U/mL)	Ei (mV)
ZrO_2	41	62
ZrO_2P25	24	−30
ZrO_2S25	2	−81
ZrO_2S25P25	15	−77
ZrO_2S50P25	0	−175
ZrO_2S25P50	0	−234
ZrO_2P25T25	37	41
ZrO_2S25T25	40	41
ZrO_2S25P25T25	77	122
ZrO_2S25P25T50	69	117
ZrO_2S50P25T25	11	−35
ZrO_2S25P50T25	15	−81

The ZrO_2S25P25, ZrO_2S25, and ZrO_2P25 samples impregnated with TPA display higher acidic strength and total number of sites than the parent supports. ZrO_2S25P25T25, ZrO_2S25P25T50, ZrO_2S25T25, and ZrO_2P25T25 present very strong acid sites with Ei > 0 mV values. No significant improvement of the acid properties was achieved in the case of the ZrO_2S50P25 and ZrO_2S25P50 supports.

XPS analyses of the HPA, supports and TPA-supported catalysts were performed to analyze the surface composition of the samples and the chemical state of the different elements. The binding energies (B.E.) of the O 1*s*, W 4*f*, P 2*p*, Si 2*p* and Zr 3*d* signals are included in Table 3.

Table 3. XPS results. Binding energies (B.E) of elements in TPA and catalysts.

Catalysts	Binding Energies (eV)				
	O 1*s*	**Si 2*p***	**W 4*f***	***Zr 3d***	**P 2*p***
TPA	531.3	-	36.3	-	134.1
	532.7		38.5		135.0
ZrO_2S25	530.2	101.8	-	182.1	-
	531.9			184.5	
	536.6			-	
ZrO_2S25T25	530.4	101.9	35.6	182.3	133.4
	531.9		37.7	184.7	134.2
	535.9				
ZrO_2S25P25	530.8	101.8	-	182.1	-
	531.7			184.5	
	536.1				
ZrO_2S25P25T25	530.4	101.9	35.6	182.3	133.1
	531.9		37.7	184.6	133.9
	535.5				
ZrO_2S25P25T50	530.9	102.4	36.0	182.7	133.8
	532.4		38.1	185.1	134.7

The Zr 3*d* core level spectra of the ZrO_2S25PYY, ZrO_2S25PYYT25 and ZrO_2S25P25T50 samples present the typical doublet at approximately 182 eV and 184 eV, corresponding to the Zr $3d_{5/2}$ and Zr $3d_{3/2}$ levels, respectively [41,42]. The observed energy difference between Zr $3d_{5/2}$ and Zr $3d_{3/2}$ (~2.4 eV) is consistent with the presence of ZrO_2-type species [43]. The values found for the Zr $3d_{5/2}$ signals (182.1–182.7 eV) are close to those reported in the literature for ZrO_2 (Zr^{4+})/Zr (IV) in an oxidic environment [44,45]. The Zr $3d_5/_2$ and Zr $3d_3/_2$ signals in the spectra of the TPA-containing catalysts (ZrO_2S25PYYT25

and ZrO_2S25P25T50 samples) shift towards a higher B.E. compared to the ZrO_2S25PYY samples. These results suggest the interaction between the zirconia and the supported acid.

For the TPA (Figure 3), the W 4*f* core level spectrum shows a well resolved doublet at 38.5 and 36.3 eV, corresponding to the W $4f_{5/2}$ and W $4f_{7/2}$ levels, respectively [46], associated with the presence of W(VI) octahedrally coordinated by oxygen. In the spectra of ZrO_2S25T25 and ZrO_2S25P25T25 samples, shown in Figure 4, W $4f_{5/2}$ and W $4f_{7/2}$ signals appear at lower B.E. (37.7 and 35.1 eV, respectively). The shift in energy values suggests a possible change or disturbance in the octahedron of oxygen atoms surrounding W [36]. This disturbance is attributed to the interaction of the Keggin structures of TPA with the support, which can be due to W-O-Zr covalent bond formation or to electrostatic interaction of the terminal oxygens (W=O) [31]. However, the disturbance could also be due to the lacunar and dimeric species present.

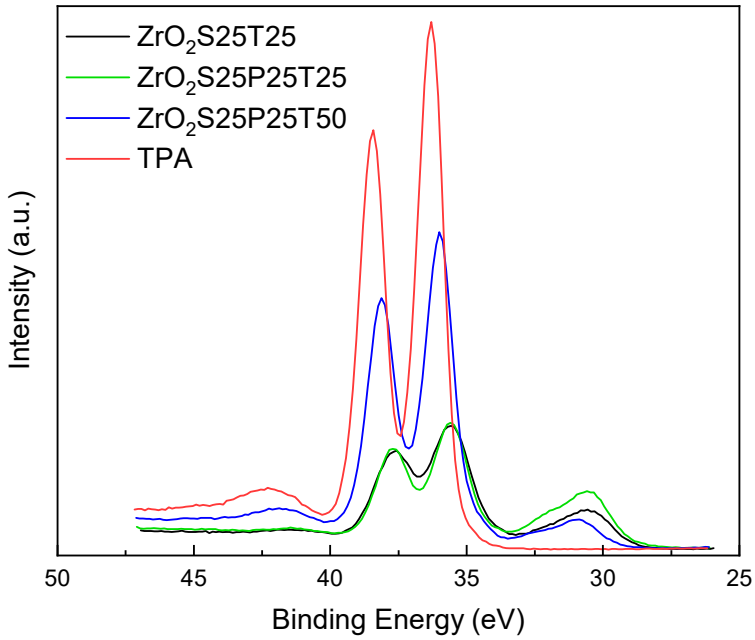

Figure 3. High-resolution W 4f XPS spectra of ZrO_2S25T25, ZrO_2S25P25T25, ZrO_2S25P25T50, and bulk TPA.

Finally, the P 2*p* core level region of the TPA spectrum shows contributions of the P $2p_{1/2}$ and P $2p_{3/2}$ levels located at ~135 and ~134 eV, respectively. These signals appear at lower B.E. in the spectra of ZrO_2S25T25 and ZrO_2S25P25T25 samples. This shift can also be observed in the spectrum of the ZrO_2S25P25T50 sample, but in this case, the shift is less evident.

The high-resolution O 1*s* spectrum of TPA shows two distinct contributions at 531.3 eV and 532.7 eV, associated with W-O-W and W-O-P bonds, respectively [47]. Meanwhile, the spectra of the supported samples also show a broad signal located at ~530.2–530.8 eV, which is typical of lattice O 1*s* in ZrO_2.

Furthermore, surface analysis reveals that silica removal from the matrix was incomplete, as the spectra show signals associated with the presence of silicon. The Si 2*p* core level signal appears at ~102–103 eV, which is attributed to silica photoemissions in an oxidic environment.

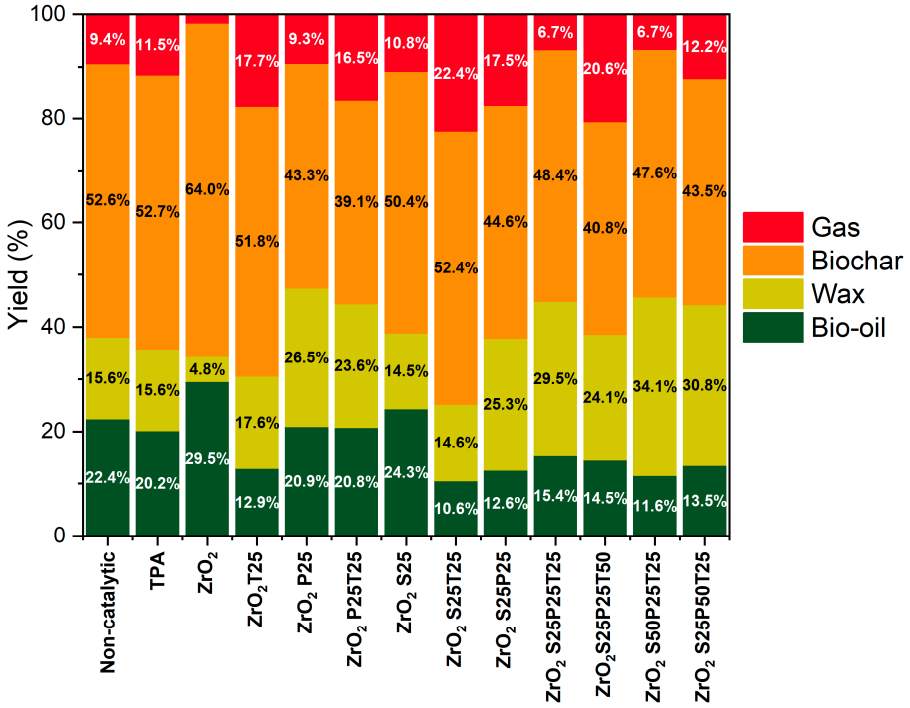

Figure 4. Effect of catalysts on the yields of each fraction obtained in pyrolysis experiments.

3.3. Catalytic Pyrolysis

3.3.1. Influence of Catalysts on Bio-Oil Composition

Figure 4 shows the percentage of each fraction obtained from the biomass pyrolysis experiments. The liquid fraction includes only the compounds that remain liquid at room temperature, while the wax fraction consists of those that volatilize during pyrolysis and subsequently solidify in the condenser. In addition to small molecules, this fraction contains condensation products, high-molecular-weight compounds, and fatty acids, among others. These waxy phases were diluted in acetone and analyzed by GC–MS to confirm the presence of such compounds. However, this fraction was not further characterized, as it fell outside the scope of the present study. Finally, the solid fraction—referred to as the biochar—comprises biochar and condensates made up of polycyclic compounds, large molecules, and other components.

The low activity observed for bulk TPA is primarily due to its extremely low surface area (<10 m^2 g^{-1}). Furthermore, in an ex situ fixed-bed configuration, bulk TPA suffers from severe mass-transfer limitations, as the evolving pyrolytic vapors cannot effectively penetrate the non-porous crystalline structure, resulting in minimal interaction compared to the high-accessibility multimodal catalysts.

As shown in Figure 4, the decisive role of the porous architecture is evident: while macropores facilitate mass transport, the introduction of mesoporosity is what truly triggers the cracking of bulky tar species. It should be noted that catalysts prepared with mesopore formers generate a higher proportion of waxes, at the expense of a lower bio-solids content.

To compare the similarities and differences in the catalytic behavior of the zirconia materials obtained in this study—where macroporous templates were incorporated during the synthesis—Figure 4 also presents results from materials prepared without these templates: ZrO_2T25, ZrO_2P25, ZrO_2P25T25, and bulk TPA. These data were previously reported in Ref. [22].

Non-catalytic pyrolysis of tomato stems and leaves yielded 22.4% bio-oils, 15.6% wax, and 52.6% biochar. The experiment performed with bulk TPA showed efficiencies that were comparable to those of the non-catalytic test, which was likely due to the low surface area

of TPA, which limited its interaction with the evolving pyrolytic gases. The low activity observed for bulk TPA is primarily due to its extremely low surface area (<10 m^2 g^{-1}). Furthermore, in an ex situ fixed-bed configuration, bulk TPA suffers from severe mass-transfer limitations, as the evolving pyrolytic vapors cannot effectively penetrate the non-porous crystalline structure, resulting in minimal interaction compared to the high-accessibility multimodal catalysts [21].

The use of ZrO_2 resulted in the highest bio-oils yield (29.5%). This material is characterized by moderate acidity and limited porosity, which favor the formation of volatile liquids without inducing excessive cracking [22]. Pyrolysis assisted by the TPA supported on ZrO_2 produced a lower bio-oils yield and a higher gas yield than non-catalytic pyrolysis. It is worth noting that the ZrO_2T25 catalyst contains well dispersed TPA on its surface and exhibits a very high acid strength (~E_0 = 684 mV, see Table 2), thereby promoting cracking reactions.

In contrast, the ZrO_2P25 material, prepared using the mesopore-forming agent P123, showed a slight increase in wax yield (26.5%) and a marked decrease in solid fraction yield (43.3%) compared to the non-catalytic test. This behavior is attributed to its high surface area (192 m^2 g^{-1}, see Table 1) and large proportion of mesopores, which enhance the accessibility of bulky tar molecules and improve the efficiency of their cracking into smaller compounds that eventually condense as waxes.

However, when this material was treated with TPA (ZrO_2P25T25), its efficiency for bio-oils production decreased significantly, favoring the formation of biochar (68.8%) and reducing the bio-oils yield to 6.7%. This behavior is attributed to its low-to-moderate acid strength (~E° = 38 mV, see Table 2) and reduced porosity resulting from TPA impregnation [22].

In this context, the present study evaluated the synthesis of zirconia with a larger pore size, using NSP-SiO_2 as a macroporous template, resulting in ZrO_2S25. Biomass pyrolysis using this material yielded 24.3% bio-oils, 14.5% waxes, and 50.4% solid residue, which are values similar to those obtained in the non-catalytic test. This catalyst exhibits very low acid strength (E° = −81.5 mV, see Table 2), which likely explains its limited catalytic effect.

In contrast, ZrO_2S25 impregnated with TPA (ZrO_2S25T25) showed a restricted bio-oils yield of 10.6% and a high gas fraction (22.4%). This behavior can be attributed to the combination of macroporosity and higher acid strength (E° = 40.9 mV), which promoted the cracking of bulky molecules and increased gas production at the expense of smaller condensable compounds.

To develop new materials combining different pore sizes, catalysts were synthesized using both mesopores and macropores templates. The ZrO_2S25P25 sample exhibited the largest surface area (see Table 1) but produced the lowest bio-oils yield (12.6%), while increasing the wax content (25.3%) and gas fraction (17.5%) compared to the other zirconias. This behavior suggests that the combination of macro- and mesopores promoted the condensation of pyrolytic gases into a waxy fraction, whereas the gases that were able to diffuse without reacting were released as part of the gas phase.

Zirconia impregnated with the lowest TPA concentration (25 wt%), ZrO_2S25P25T25, displayed a marked decrease in gas yield (6.7%). This indicates that the pyrolysis gases could combine more effectively, possibly facilitated by the moderately strong acid sites of this system (E° = 121.6 mV), resulting in a slight increase in the bio-oils and wax fractions.

By contrast, the ZrO_2S25P25T_{50} catalyst produced lower amounts of bio-oils, wax, and biochar (14.5%, 24.1%, and 40.8%, respectively) and a substantial increase in gases (20.6%). Although this material exhibited similar acidic properties to ZrO_2S25P25T25 (see entries 8 and 9 in Table 2), the distribution of pyrolysis fractions differed, which was likely due to a higher density of active sites per unit area.

Finally, tests with synthesized catalysts using higher amounts of pore formers, such as ZrO_2S50P25T25 and ZrO_2S25P50T25, showed comparable efficiencies. These materials were notable for producing high wax yields (34.1% and 30.8%, respectively) without significantly increasing bio-oils production (11.6% and 13.5%, respectively). The combination of meso- and macroporous structures with low acidity likely promoted the formation of heavy compounds that were not cracked on the catalyst surface and subsequently condensed as waxes [48].

Although these multimodal materials exhibited lower bio-oils yields than the non-catalytic test, the results underscore the significant influence of both catalyst acidity and pore architecture on the quantity and characteristics of the condensable products, highlighting the importance of rational catalyst design to optimize the production of the desired fraction.

3.3.2. Influence of Catalysts on the Composition of Bio-Oil

As previously reported, the bio-oils obtained in the presence of mesoporous catalysts—TPA, ZrO_2, ZrO_2T25, ZrO_2P25, and ZrO_2P25T25—exhibited a higher concentration of C5 and C6 molecules compared to the non-catalytic sample, which predominantly produced C2 compounds. The most abundant C5 species were furanic compounds, including furfural and furfuryl alcohol (FA), as well as aldehydes and ketones such as pentanal and 1,2-cyclopentanedione. The main C6 molecule detected was the anhydro sugar dianhydroglucopyranose (DAGP). These results clearly indicate that the presence of catalysts promotes the formation of valuable molecules for biorefinery-related applications.

Figure 5a,b illustrate the distribution of compounds in the bio-oils obtained from the catalytic and non-catalytic pyrolysis of tomato plant waste (leaves and stems). Figure 5a highlights the influence of catalysts on the relative content of different compound families in the pyrolytic bio-oils, while Figure 5b shows the impact of catalysts on the relative abundance of individual molecules. As observed, catalytic tests significantly affect the composition of the resulting bio-oils.

The bio-oils from non-catalytic pyrolysis exhibited an oxygen-rich profile, consisting of 27.1% carboxylic acids (including acetic and formic acids), 35.9% ketones (predominantly hydroxyacetone, 2,3-butanedione, and cyclopentanone), and 10.4% furan compounds (furfural and 2(5*H*)-furanone). Additionally, it contained 10.1% nitrogen compounds, primarily a pyridine derivative, and a small amount of diols (3.6%), including ethylene glycol. This composition is consistent with reports for the pyrolysis of similar biomasses, such as corn cobs and certain grasses [49,50]. These bio-oils are rich in diverse oxygenated compounds, making separation difficult and limiting their commercial value [27].

Figure 5a shows that pyrolysis performed in the presence of multimodal catalysts—catalysts combining meso- and macropores—generated bio-oils with a lower number of organic compound families, demonstrating a more effective combination of pyrolytic gases.

While acetic acid was the most abundant molecule in almost all bio-oils (Figure 5b) formed through the cleavage of terminal acetyl groups from hemicellulose polymer chains [51], the results obtained with multimodal catalysts revealed an interesting but limited distribution of products. These products primarily belong to the families of acids, ketones, and aldehydes. Furan compounds and esters are present to a lesser extent. This highlights the strong influence of the catalysts on the selectivity toward these compound families.

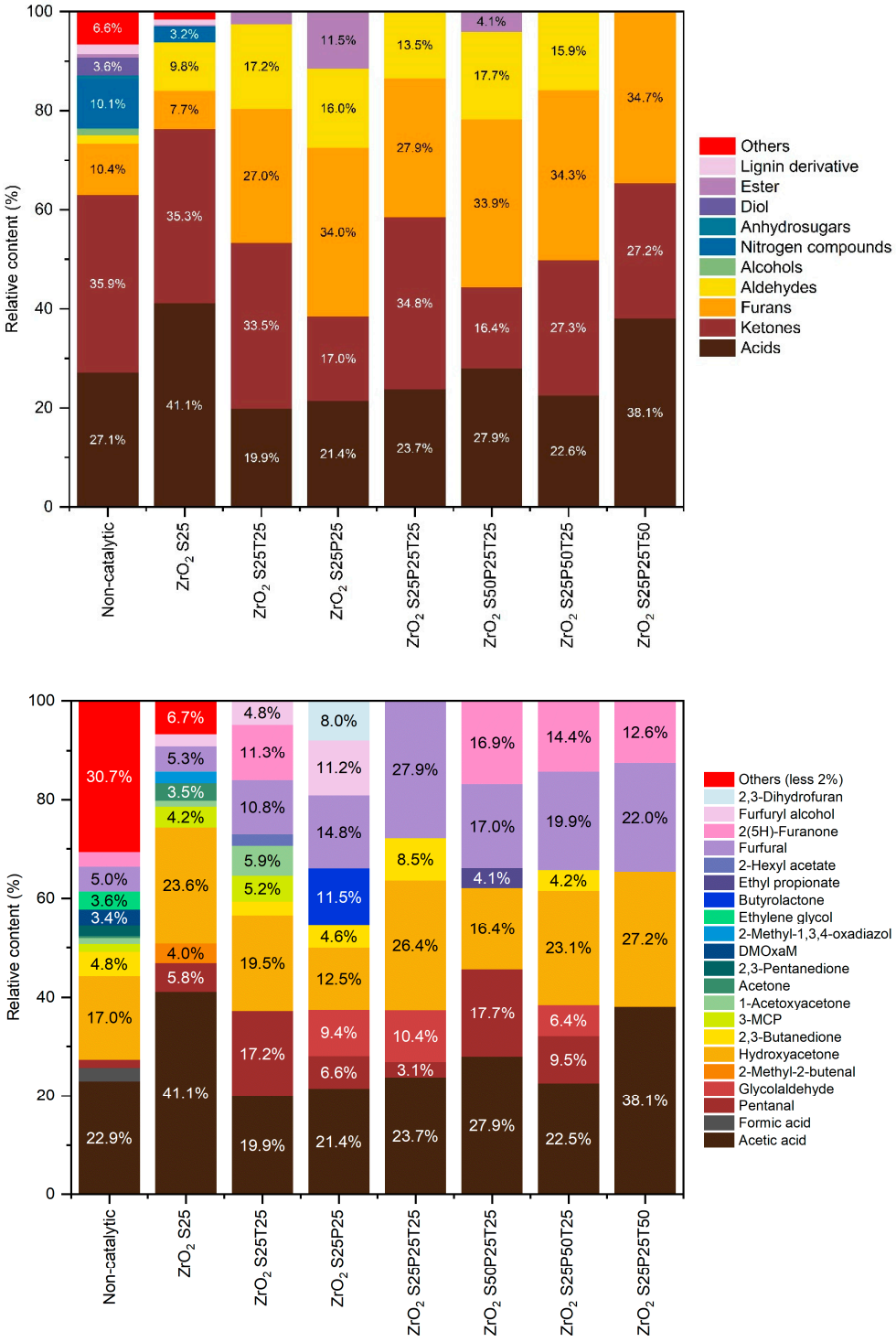

Figure 5. (**a**) Influence of the presence of catalysts on the relative content of different compound families in the obtained pyrolytic bio-oils. (**b**) Influence of the presence of catalysts on the compounds present in bio-oils.

The ZrO_2S25 support, synthesized with silica nanospheres as the sole pore former, produced bio-oils containing the highest concentrations of acids (41.1%) and ketones (35.3%) compared to the non-catalytic test. Acetic acid was the only acid detected, while the ketones included hydroxyacetone, 2,3-butanedione, acetoxyacetone, and cyclopentanone. The presence of macropores in the catalyst likely facilitated the entry of larger molecules, promoting sugar ring-opening reactions and/or protein degradation. This resulted in lower concentrations of furans and nitrogenous compounds compared to the non-catalytic test [52].

The ZrO_2S25T25 catalyst, prepared by impregnating the aforementioned support with TPA, promoted a higher proportion of furan compounds (27%) and aldehydes (17.2%), while reducing acid formation to 19.9% (see Figure 5a). This indicates that the acidic sites in the material favored glycosidic bond cleavage and sugar dehydration reactions, generating furfural, 2(5*H*)-furanone, furfuryl alcohol, and pentanal (see Figure 5b).

Among the bio-oils obtained, the lowest selectivity toward a limited number of molecules was observed for the pyrolysis test using the ZrO_2S25P25 support, which contains both macro- and mesopores. These bio-oils exhibited significant concentrations of furans (34%), including furfural, furfuryl alcohol, and 2,3-dihydrofuran, as well as aldehydes (16%). The combined presence of macro- and mesopores likely promotes dehydration and/or hydrolysis pathways [53,54].

Catalytic tests performed using ZrO_2SXXPYY impregnated with TPA, such as ZrO_2S25P25T25, ZrO_2S50P25T25, and ZrO_2S25P50T25, yielded similar results, producing bio-oils with a limited number of products. Notably, the composition of these bio-oils was reduced to five or fewer compound families compared to the non-catalytic test. For example, the ZrO_2S25P25T25 catalyst, characterized by a meso-macropore architecture and moderate acid properties, produced concentrations of acids and ketones that were comparable to the non-catalytic sample, while promoting the formation of furfural as the sole furanic compound at a high concentration (~27.9%), along with aldehydes (13.5%). Among the aldehydes, the formation of pentanal from the lignin fraction and of glycolaldehyde, present in low concentrations from the secondary cleavage of levoglucosan and/or cyclopentanone, was notable [55]. These results demonstrate that a favorable structural and chemical balance promoted the generation of selective bio-oils with limited molecular diversity [55]. The ketone fraction was dominated by hydroxyacetone (26.4%), with a smaller proportion of 2,3-butanedione also present (see Figure 5b).

On the other hand, ZrO_2S25P50T25 and ZrO_2S50P25T25 samples produced bio-oils with similar profiles and were highly selective toward the formation of furans and aldehydes compared to the non-catalytic test. In Figure 5b, the furans identified in both bio-oils were furfural and its oxidation product, 2(5*H*)-furanone, possibly formed at the redox sites of zirconia. Ketone production was 16.4%, exclusively as hydroxyacetone, for ZrO_2S50P25T25, and 27.3%, distributed between hydroxyacetone and 2,3-butanedione, for ZrO_2S25P50T25. This behavior is likely associated with the V_p of the materials; for instance, ZrO_2S50P25T25 had a V_p of 0.25 $cm^3\ g^{-1}$, whereas ZrO_2S25P50T25 exhibited a higher V_p of 0.45 $cm^3\ g^{-1}$ (see Table 1).

Finally, the ZrO_2S25P25T50 sample, characterized by the highest TPA loading, promoted the formation of a large proportion of acids (38.1%) and furanic compounds (34.7%), accompanied by a moderate ketone content (27.2%). Notably, the composition of these bio-oils was limited to only three compound families, suggesting that multimodal systems with effective acid activity can exert selective control over the distribution of products.

In summary, multimodal catalysts impregnated with TPA improved the selectivity towards organic compounds of interest, such as furfural. However, high concentrations of TPA (ZrO_2S25P25T50) generated large quantities of acetic acid (38.1%), furfural, and its catalytic oxidation product (2(5H)-furanone). These tests determined that the optimal meso/macropore and acidity ratio for obtaining 27.9% furfural was achieved with the catalyst synthesized with ZrO_2S25P25T25. In general, bio-oils obtained from pyrolysis tests using the synthesized catalysts exhibited clear selectivity toward specific compounds, influenced by the catalysts' architecture and/or acidity. The structure–function relationship is further confirmed; the hierarchical combination of meso- and macropores not only increases yield but acts as a molecular filter, effectively reducing the number of chemical families to just three or five in the TPA-functionalized systems.

4. Conclusions

In this study, catalysts composed of tungstophosphoric acid (TPA) supported on meso-macroporous zirconia were synthesized through the sol–gel method. A comprehensive characterization of the materials was conducted using diverse analytical techniques. The primary findings of this study demonstrate a significant correlation between the ZrO_2SXXPYY S_{BET} and D_p parameters and the amount of NSP-SiO_2 (SXX) and P123 (PYY) utilized during the synthesis process. Furthermore, the FT-IR, NMR-MAS, and XRD results indicated the presence of $[PW_{12}O_{40}]^{3-}$, $[P_2W_{21}O_{71}]^{6-}$, and $[PW_{11}O_{39}]^{7-}$ anions dispersed on the zirconia support.

The results of the catalytic pyrolysis of tomato residues have demonstrated that the porous architecture of the catalyst and the presence of TPA play a pivotal role in determining the distribution of the resulting fractions. While non-catalytic pyrolysis and the macroporous support ZrO_2 S25 exhibited comparable bio-oil yields (approximately 22–24%), the introduction of mesoporosity facilitated the cracking of bulky tar species, thereby increasing the yields of the gas and wax fractions. These results provide evidence that the combination of macropores, which enhance mass transport, and mesopores, which provide active surface area, minimizes biochar formation and improves the release of volatile species compared to conventional porous configurations.

Additionally, the incorporation of tungstophosphoric acid (TPA) proved to be pivotal in modulating the bio-oil's composition. The chemical evolution is driven by the catalyst's high strength acid and site density, which act as the primary drivers for selective dehydration and cracking pathways. The multimodal meso-macroporous architecture ensures the effective transport and accessibility of bulky tar molecules to these active sites. The efficacy of this rational design is evidenced by the performance of the ZrO_2 S25P25 system, which achieved a furan content of 34%, and the substantial reduction in molecular diversity attained with ZrO_2 S25P25T25 and ZrO2 S25P25T50 catalysts, constraining the bio-oil to a mere five and three chemical families, respectively.

A comprehensive analysis of the findings of this research reveals that the synergistic interplay between a meticulously designed multimodal structure and controlled acidity constitutes an effective strategy for directing pyrolysis toward products with reduced complexity and higher industrial value. Subsequent investigations will concentrate on the evaluation of the long-term stability and reusability of these catalysts. This evaluation will include detailed leaching and deactivation studies, in order to assess their potential for large-scale and continuous pyrolysis operations.

Supplementary Materials: The following supporting information can be downloaded at: https://www.mdpi.com/article/10.3390/reactions7010021/s1, Figure S1. Schematic diagram of the experimental setup for the ex situ catalytic pyrolysis of tomato plant residues. Figure S2. N2 adsorption–desorption isotherm ZrO2, ZrO2 T25, ZrO2 P25, ZrO2 P25T25, ZrO2 S25, ZrO2 S25 T25, ZrO2 S25P25, ZrO2 S25P25T25, ZrO2 S25P25T50, ZrO2 S50P25, ZrO2 S50P25T25 ZrO2 S25P50 and ZrO2 S25P50T25. Figure S3. Pore size distribution ZrO2, ZrO2 P25, ZrO2 S25, ZrO2 S25P25, ZrO2 S50P25 and ZrO2 S25P50. Table S1. Textural properties and surface area reduction percentage (SBET drop %) of the synthesized materials. Table S2. Surface Na/Si atomic ratios of the ZrO2S25, ZrO2S25T25, ZrO2S25P25, ZrO2S25P25T25, and ZrO2S25P25T50 materials determined by XPS. Figure S4. FT-IR spectrum of synthesized materials. Figure S5. Potentiometric titration curves of synthesized materials. References [56,57] have been mentioned in the text.

Author Contributions: Conceptualization, M.L.C., I.D.L. and L.R.P.; methodology, L.R.P. and I.D.L.; formal analysis, J.L.B., L.J.M. and J.A.C.; data curation, L.J.M. and J.A.C.; writing—original draft preparation, J.L.B. and L.J.M.; writing—review and editing, all authors; supervision, E.R.-C., M.L.C., L.R.P. and I.D.L.; funding acquisition, M.L.C., E.R.-C., I.D.L. and. L.R.P. All authors have read and agreed to the published version of the manuscript.

Funding: This research was funded by the Consejo Nacional de Investigaciones Científicas y Técnicas-CONICET (Grant PUE 00572018, PIP086, PIP 1492), Universidad Nacional de La Plata-UNLP (Grant 11/X903), CIC-PROINGED (Ciencia y Tecnología en Energías Bonaerenses) and Agencia Nacional de Promoción de la Investigación, el Desarrollo Tecnológico y la Innovación-Agencia i+D+i (Grant PICT 1830 and PICT AI601/2021), and Spanish Agencia Estatal de Investigación (PID2021-125762NB-100) and Gobierno de Aragón (E7_23R group). J.A. Cecilia and E. Rodríguez-Castellón thank project PID2021-126235OB-C32, funded by MCIN/AEI/10.13039/501100011033/ and FEDER funds.

Data Availability Statement: Data are contained within the article.

Acknowledgments: The authors acknowledge the financial support of CONICET, ANPCyT, and UNLP, and María Laura Barbelli, Alexis Sosa, and Hernán Bideberripe for their collaborations. The authors thank Universidad de Buenos Aires (UBA), Argentina; Universidad Nacional de La Plata (UNLP), Argentina; ICMA, Instituto de Síntesis Química y Catálisis Homogénea (ISQCH), CSIC-Universidad de Zaragoza, España; and Consejo Nacional de Investigaciones Científicas y Técnicas"-CONICET and "Agencia Nacional de Promoción de la Investigación, el Desarrollo Tecnológico y la Innovación" for their financial and scientific support.

Conflicts of Interest: The authors declare no conflicts of interest.

Abbreviations

The following abbreviations are used in this manuscript:

FT-IR	Fourier Transform Infrared Spectrometry
HPAs	Heteropolyacids
S_{BET}	Specific Surface Area
SEM	Scanning Electron Microscopy
S_{MIC}	Micropore Specific Surface Area
TPA	Tungstophosphoric Acid
V_p	Total Pore Volume
D_p	Pore Diameter
Ei	Initial Electrode Potential
N_{AS}	Number of Acid Sites

References

1. Mouganie, P.; Ajeeb, R.; Hoekstra, M. *The Effect of Open-Air Waste Burning on Infant Health: Evidence from Government Failure in Lebanon*; National Bureau of Economic Research: Cambridge, MA, USA, 2020. Available online: https://www.nber.org/system/files/working_papers/w26835/w26835.pdf (accessed on 20 November 2024).
2. Andini, A.; Bonnet, S.; Rousset, P.; Hasanudin, U. Impact of Open Burning of Crop Residues on Air Pollution and Climate Change in Indonesia. *Curr. Sci.* **2018**, *115*, 2259–2266. [CrossRef]
3. Wang, H.; Yang, B.; Zhang, Q.; Zhu, W. Catalytic Routes for the Conversion of Lignocellulosic Biomass to Aviation Fuel Range Hydrocarbons. *Renew. Sustain. Energy Rev.* **2020**, *120*, 109612. [CrossRef]
4. Tiwari, J.K.; Behera, T.K.; Rai, N.; Yerasu, S.R.; Singh, M.K.; Singh, P.M. Tomato Breeding for Processing in India: Current Status and Prospects. *Veg. Sci.* **2022**, *49*, 123–132. [CrossRef]
5. Almeida, P.V.; Rodrigues, R.P.; Gaspar, M.C.; Braga, M.E.M.; Quina, M.J. Integrated Management of Residues from Tomato Production: Recovery of Value-Added Compounds and Biogas Production in the Biorefinery Context. *J. Environ. Manag.* **2021**, *299*, 113505–113511. [CrossRef]
6. Food and Agriculture Organization of the United Nations (FAO) Statistics | FAO. Available online: http://www.fao.org/ecosystem-services-biodiversity/background/supporting-services/en/ (accessed on 22 June 2025).

7. Chang, J.M.; Joye, I.J. Improving Agricultural Sustainability—A Review of Strategies to Valorize Tomato Plant Residues (TPR). *Waste Manag.* **2024**, *190*, 88–101. [CrossRef]
8. Panchasara, H.; Ashwath, N. Effects of Pyrolysis Bio-Oils on Fuel Atomisation—A Review. *Energies* **2021**, *14*, 794. [CrossRef]
9. Dickerson, T.; Soria, J. Catalytic Fast Pyrolysis: A Review. *Energies* **2013**, *6*, 514–538. [CrossRef]
10. Collard, F.-X.; Blin, J. A Review on Pyrolysis of Biomass Constituents: Mechanisms and Composition of the Products Obtained from the Conversion of Cellulose, Hemicelluloses and Lignin. *Renew. Sustain. Energy Rev.* **2014**, *38*, 594–608. [CrossRef]
11. Kumar, A.; Kumari, L.; Laghari, A.A.; Rong, H.; Jamro, I.A.; Sajnani, S.; Aborisade, M.A.; Rajput, G.; Oba, B.T.; Nkinahamira, F.; et al. Exploring the Integrated Potential of Pyrolysis and Low-Temperature Wet Torrefaction for Typical Medical Waste Valorization: A Multifaceted Approach Leveraging Online TG-FTIR-MS, 2D-COS, Iso-Conversional Kinetics, and Reaction Mechanisms. *Chem. Eng. J.* **2024**, *499*, 156464. [CrossRef]
12. Wang, K.; Johnston, P.A.; Brown, R.C. Comparison of In-Situ and Ex-Situ Catalytic Pyrolysis in a Micro-Reactor System. *Bioresour. Technol.* **2014**, *173*, 124–131. [CrossRef] [PubMed]
13. de Rezende Locatel, W. *Valorization of Waste Biomass by Catalytic Pyrolysis*; Université de Lyon: Lyon, France, 2022.
14. Chen, X.; Yang, H.; Chen, Y.; Chen, W.; Lei, T.; Zhang, W.; Chen, H. Catalytic Fast Pyrolysis of Biomass to Produce Furfural Using Heterogeneous Catalysts. *J. Anal. Appl. Pyrolysis* **2017**, *127*, 292–298. [CrossRef]
15. Duan, D.; Chen, D.; Huang, L.; Zhang, Y.; Zhang, Y.; Wang, Q.; Xiao, G.; Zhang, W.; Lei, H.; Ruan, R. Activated Carbon from Lignocellulosic Biomass as Catalyst: A Review of the Applications in Fast Pyrolysis Process. *J. Anal. Appl. Pyrolysis* **2021**, *158*, 105246. [CrossRef]
16. Bielański, A.; Lubańska, A. FTIR Investigation on Wells-Dawson and Keggin Type Heteropolyacids: Dehydration and Ethanol Sorption. *J. Mol. Catal. A Chem.* **2004**, *224*, 179–187. [CrossRef]
17. Jin, Y.; Liu, S.; Shi, Z.; Wang, S.; Wen, Y.; Zaini, I.N.; Tang, C.; Hedenqvist, M.S.; Lu, X.; Kawi, S.; et al. A Novel Three-Stage Ex-Situ Catalytic Pyrolysis Process for Improved Bio-Oil Yield and Quality from Lignocellulosic Biomass. *Energy* **2024**, *295*, 131029. [CrossRef]
18. Hernando, H.; Hernández-Giménez, A.M.; Gutiérrez-Rubio, S.; Fakin, T.; Horvat, A.; Danisi, R.M.; Pizarro, P.; Fermoso, J.; Heracleous, E.; Bruijnincx, P.C.A.; et al. Scaling-Up of Bio-Oil Upgrading during Biomass Pyrolysis over ZrO_2/ZSM-5-Attapulgite. *ChemSusChem* **2019**, *12*, 2428–2438. [CrossRef]
19. Font, R.; Moltó, J.; Gálvez, A.; Rey, M.D. Kinetic Study of the Pyrolysis and Combustion of Tomato Plant. *J. Anal. Appl. Pyrolysis* **2008**, *85*, 268–275. [CrossRef]
20. Ozbay, N.; Yargic, A.S.; Yarbay Sahin, R.Z. Tailoring Cu/Al2O3 Catalysts for the Catalytic Pyrolysis of Tomato Waste. *J. Energy Inst.* **2018**, *91*, 424–433. [CrossRef]
21. Özbay, N.; Yargiç, A.S.; Yarbay Şahin, R.Z.; Yaman, E. Research on the Pyrolysis Characteristics of Tomato Waste With Fe-Al_2O_3 Catalyst. In *Exergetic, Energetic and Environmental Dimensions*; Elsevier Inc.: Amsterdam, The Netherlands, 2018; pp. 815–828, ISBN 9780128137352.
22. Buitrago, J.L.; Méndez, L.J.; Musci, J.J.; Cecilia, J.A.; Ballesteros-Plata, D.; Rodríguez-Castellón, E.; Casella, M.L.; Pizzio, L.R.; Lick, I.D. Obtention and Products Distribution of Bio-oils from Catalytic Pyrolysis of Tomato Plant Waste. *Catalysts* **2025**, *15*, 388. [CrossRef]
23. Stöber, W.; Fink, A. Controlled Growth of Monodisperse Silica Spheres in the Micron Size Range. *J. Colloid Interface Sci.* **1968**, *26*, 62–69. [CrossRef]
24. Goering, H.K.; Van Soest, P.J. *Forage Fiber Analysis: Apparatus, Reagents, Procedures and Some Applications*; United States Agricultural Research Service: Washington, DC, USA, 1970; Volume 379, pp. 1–20.
25. Holtzapple, M.T. Cellulose. In *Encyclopedia of Food Sciences and Nutrition*; Academic Press: Cambridge, MA, USA, 2003; pp. 998–1007.
26. Liu, Y.; Wu, S.; Zhang, H.; Xiao, R. Fast Pyrolysis of Holocellulose for the Preparation of Long-Chain Ether Fuel Precursors: Effect of Holocellulose Types. *Bioresour. Technol.* **2021**, *338*, 125519. [CrossRef] [PubMed]
27. Venderbosch, R.H. A Critical View on Catalytic Pyrolysis of Biomass. *ChemSusChem* **2015**, *8*, 1306–1316. [CrossRef]
28. Kok, M.V.; Ozgur, E. Characterization of Lignocellulose Biomass and Model Compounds by Thermogravimetry. *Energy Sources Part A Recovery Util. Environ. Eff.* **2017**, *39*, 134–139. [CrossRef]
29. Vitas, S.; Segmehl, J.S.; Burgert, I.; Cabane, E. Porosity and Pore Size Distribution of Native and Delignified Beech Wood Determined by Mercury Intrusion Porosimetry. *Materials* **2019**, *12*, 416. [CrossRef] [PubMed]
30. Thommes, M.; Kaneko, K.; Neimark, A.V.; Olivier, J.P.; Rodriguez-Reinoso, F.; Rouquerol, J.; Sing, K.S.W. Physisorption of gases, with special reference to the evaluation of surface area and pore size distribution (IUPAC Technical Report). *Pure Appl. Chem.* **2015**, *87*, 1051–1069. [CrossRef]

31. Aguilera, E.X.; Sathicq, Á.G.; Sosa, A.; Murguía, M.C.; Martínez, J.J.; Pizzio, L.R.; Romanelli, G.P. Mesostructured Silica–Zirconia–Tungstophosphoric Acid Composites as Catalyst in Calcium Channel Blocker Nifedipine Synthesis. *Catalysts* **2025**, *15*, 537. [CrossRef]
32. Dong, H.; Luo, W.; Yan, X.; Li, B.; Hu, J.; Huang, S.; Xia, M.; Zhong, M.; Tang, Q.; Zhou, Z.; et al. Production of Catalytic-Upgraded Pyrolysis Products from Oiltea Camellia Shell and Polypropylene Using NiCe-X/Al_2O_3 and ZrO_2 Catalyst (X = Fe, Co). *Fuel* **2022**, *325*, 124812. [CrossRef]
33. Su, Y.L.; Wang, J.; Liu, H.Z. FTIR Spectroscopic Study on Effects of Temperature and Polymer Composition on the Structural Properties of PEO-PPO-PEO Block Copolymer Micelles. *Langmuir* **2002**, *18*, 5370–5374. [CrossRef]
34. Fuchs, V.; Méndez, L.; Blanco, M.; Pizzio, L. Mesoporous Titania Directly Modified with Tungstophosphoric Acid: Synthesis, Characterization and Catalytic Evaluation. *Appl. Catal. A Gen.* **2009**, *358*, 73–78. [CrossRef]
35. Lefebvre, F. ^{31}P MAS NMR Study of $H_3PW_{12}O_{40}$ Supported on Silica: Formation of $(SiOH_2^+)(H_2PW_{12}O_{40}^-)$. *J. Chem. Soc. Chem. Commun.* **1992**, *10*, 756–757. [CrossRef]
36. Legagneux, N.; Basset, J.-M.; Thomas, A.; Lefebvre, F.; Goguet, A.; Sá, J.; Hardacre, C. Characterization of Silica-Supported Dodecatungstic Heteropolyacids as a Function of Their Dehydroxylation Temperature. *Dalton Trans.* **2009**, *12*, 2235–2240. [CrossRef]
37. Pope, M.T. *1933-Heteropoly and Isopoly Oxometalates*, 1st ed.; Springer: Berlin/Heidelberg, Germany, 1983; ISBN 9783662120064.
38. Pizzio, L.R.; Cáceres, C.V.; Blanco, M.N. Acid catalysts prepared by impregnation of tungstophosphoric acid solutions on different supports. *Appl. Catal. A Gen.* **1998**, *167*, 283–294. [CrossRef]
39. Li, H.; Ren, J.; Qin, X.; Qin, Z.; Lin, J.; Li, Z. Ni/SBA-15 Catalysts for CO Methanation: Effects of V, Ce, and Zr Promoters. *RSC Adv.* **2015**, *5*, 96504–96517. [CrossRef]
40. Wang, L.; Yang, J. Zirconia-Doped Methylated Silica Membranes via Sol-Gel Process: Microstructure and Hydrogen Permselectivity. *Nanomaterials* **2022**, *12*, 2159. [CrossRef] [PubMed]
41. Ardizzone, S.; Bianchi, C.L. XPS characterization of sulphated zirconia catalysts: The role of iron. *Surf. Interface Anal.* **2000**, *30*, 77–80. [CrossRef]
42. Yang, G.; Wang, L.; Jiang, H. Zr-Incorporating SBA-15 for Conversion of the Ethanol-Acetaldehyde Mixture to Butadiene. *React. Chem. Eng.* **2020**, *5*, 1833–1844. [CrossRef]
43. Lackner, P.; Zou, Z.; Mayr, S.; Diebold, U.; Schmid, M. Using Photoelectron Spectroscopy to Observe Oxygen Spillover to Zirconia. *Phys. Chem. Chem. Phys.* **2019**, *21*, 17613–17620. [CrossRef]
44. You, X.; Yu, L.L.; Xiao, F.F.; Wu, S.-C.; Yang, C.; Cheng, J.-H. Synthesis of Phosphotungstic Acid-Supported Bimodal Mesoporous Silica-Based Catalyst for Defluorination of Aqueous Perfluorooctanoic Acid under Vacuum UV Irradiation. *Chem. Eng. J.* **2018**, *335*, 812–821. [CrossRef]
45. Morales, M.D.; Infantes-Molina, A.; Lázaro-Martínez, J.M.; Romanelli, G.P.; Pizzio, L.R.; Rodríguez-Castellón, E. Heterogeneous Acid Catalysts Prepared by Immobilization of H3PW12O40 on Silica through Impregnation and Inclusion, Applied to the Synthesis of 3H-1,5-Benzodiazepines. *Mol. Catal.* **2020**, *485*, 110842. [CrossRef]
46. Norouzi, O.; Taghavi, S.; Arku, P.; Jafarian, S.; Signoretto, M.; Dutta, A. What Is the Best Catalyst for Biomass Pyrolysis? *J. Anal. Appl. Pyrolysis* **2021**, *158*, 105280. [CrossRef]
47. Oh, S.-J.; Choi, G.-G.; Kim, J.-S. Production of Acetic Acid-Rich Bio-Oils from the Fast Pyrolysis of Biomass and Synthesis of Calcium Magnesium Acetate Deicer. *J. Anal. Appl. Pyrolysis* **2017**, *124*, 122–129. [CrossRef]
48. Silveira Junior, E.G.; Silveira, T.d.C.; Perez, V.H.; Justo, O.R.; David, G.F.; Fernandes, S.A. Fast Pyrolysis of Elephant Grass: Intensification of Levoglucosan Yield and Other Value-Added Pyrolytic by-Products. *J. Energy Inst.* **2022**, *101*, 254–264. [CrossRef]
49. Nachenius, R.W.; Ronsse, F.; Venderbosch, R.H.; Prins, W. Biomass Pyrolysis. In *Advances in Chemical Engineering*; Academic Press Inc.: Cambridge, MA, USA, 2013; Volume 42, pp. 75–139.
50. Liu, Y.; Wu, S.; Zhang, H.; Xiao, R. Catalytic Fast Pyrolysis of Steam-Exploded Biomass for Long-Chain Ethers Precursors. *Fuel Process. Technol.* **2022**, *235*, 107367. [CrossRef]
51. Mardiana, S.; Azhari, N.J.; Ilmi, T.; Kadja, G.T.M. Hierarchical Zeolite for Biomass Conversion to Biofuel: A Review. *Fuel* **2022**, *309*, 122119. [CrossRef]
52. Neumann, G.T.; Hicks, J.C. Novel Hierarchical Cerium-Incorporated MFI Zeolite Catalysts for the Catalytic Fast Pyrolysis of Lignocellulosic Biomass. *ACS Catal.* **2012**, *2*, 642–646. [CrossRef]
53. Xie, W.; Zhang, Y.; Zhang, Y.; Liu, C.; Wang, Y.; Xie, Y.; Ji, G.; Li, A. Fast Pyrolysis of Biomass with Diverse Properties to Produce Liquid Hydrogen Storage Molecules. *Carbon Capture Sci. Technol.* **2024**, *12*, 100230. [CrossRef]
54. Shao, S.; Liu, C.; Xiang, X.; Li, X.; Zhang, H.; Xiao, R. Insight into the Selective Production of Aldehydes and Ketones by Catalytic Upgrading of Biomass Pyrolysis Vapor over ZrO_2:Cellulose and Xylan. *Biomass Bioenergy* **2022**, *162*, 106473. [CrossRef]
55. Zhu, Y.; Li, W.; Huang, Y.; Zheng, Y.; Wang, D.; Ye, Y.; Li, S.; Zheng, Z. Catalytic Pyrolysis of Cellulose over Solid Acidic Catalysts: An Environment-Friendly Method for Furan Production. *Biomass Convers. Biorefin.* **2020**, *11*, 2695–2702. [CrossRef]

56. Fuchs, V.M.; Pizzio, L.R.; Blanco, M.N. Synthesis and Characterization of Aluminum or Copper Tungstophosphate and Tungstosilicate Immobilized in a Polymeric Blend. *Eur. Polym. J.* **2007**, *44*, 801–807. [CrossRef]
57. Cid, R.; Pecchi, G. Potentiometric Method for Determining the Number and Relative Strength of Acid Sites in Colored Catalysts. *Appl. Catal.* **1985**, *14*, 15–21. [CrossRef]